Available online at www.sciencedirect.com
SCIENCE DIRECT®
Computer Physics Communications 164 (2004) 220–228
Computer Physics Communications
www.elsevier.com/locate/cpc

3D adaptive mesh refinement simulations of pellet injection in tokamaks

R. Samtaney [a,*], S.C. Jardin [a], P. Colella [b], D.F. Martin [b]

[a] *Princeton Plasma Physics Laboratory, Princeton, NJ 08543, USA*
[b] *Lawrence Berkeley National Laboratory, Berkeley, CA 94720, USA*

Available online 21 July 2004

Abstract

We present results of Adaptive Mesh Refinement (AMR) simulations of the pellet injection process, a proven method of refueling tokamaks. AMR is a computationally efficient way to provide the resolution required to simulate realistic pellet sizes relative to device dimensions. The mathematical model comprises of single-fluid MHD equations with source terms in the continuity equation along with a pellet ablation rate model. The numerical method developed is an explicit unsplit upwinding treatment of the 8-wave formulation, coupled with a MAC projection method to enforce the solenoidal property of the magnetic field. The Chombo framework is used for AMR. The role of the $E \times B$ drift in mass redistribution during inside and outside pellet injections is emphasized.

PACS: 52.30.Cv; 52.65.Kj

Keywords: Adaptive Mesh Refinement; MHD; Pellet injection

1. Introduction

Injecting small pellets of frozen hydrogen into a tokamak is a proven method of fueling. Experimentally, it is known that the density distribution, after the pellet ablates upon encountering the high temperatures in a tokamak, is not consistent with the distribution inferred from assuming that the ablated material remains on the flux surfaces where the ablation occurred. The subsequent redistribution of mass is believed to be due to anomalous MHD processes. The mass redistribution is observed to be a sensitive function of the angle (with respect to the mid-plane) in which the pellet is injected [1,2]. It is this phenomenon which we seek to explain.

A previous three-dimensional computational investigation of pellet injection was performed by Strauss and Park [3]. They investigated the evolution of a large density "blob" representing the ionized pellet ablation cloud. However, they did not treat a moving pellet source and their resolution was relatively coarse. Our approach is to perform detailed simulations of the pellet injection process and quantify the MHD processes responsible for mass

* Corresponding author.
E-mail address: rsamtaney@pppl.gov (R. Samtaney).

0010-4655/$ – see front matter
doi:10.1016/j.cpc.2004.06.032

redistribution. We employ Adaptive Mesh Refinement (AMR) in our simulations to provide the resolution required to simulate realistic pellet sizes relative to device dimensions (typical ratios are $O(10^{-3})$). In Section 2, we describe the physical problem and the mathematical model along with the pellet ablation model and discussion of initial and boundary conditions. In Section 3, we describe the numerical method. In Section 4, we present results from AMR simulations emphasizing the differences between inside and outside injections.

2. Description of problem and mathematical model

2.1. Physical problem

The physical problem we are dealing with involves the injection of frozen fuel pellets into a tokamak. The physical processes are broadly distinguished into the following two stages. The first stage is the ablation of mass at the pellet surface due to the high temperature background plasma encountered by the pellet. The ablated pellet mass, which is a neutral gas, is rapidly heated by electrons and ionizes to form plasma. The second stage is the redistribution of the ablated pellet material by free streaming along the magnetic field lines and by anomalous MHD processes which cause mass flow across field lines and flux surfaces. The pellet ablation phenomenon of the first stage is considered well-understood [4,5], and as such we use existing ablation models. The thrust of the work described here is an accurate and efficient simulation of the second phase.

2.2. Mathematical model

Our mathematical model consists of single fluid MHD equations with source terms in the continuity equation to model the mass injected into the system by the pellet, and source (sink) terms in the energy equations to model electron heating and corresponding cooling on flux surfaces. The equations are written below.

$$\frac{\partial U}{\partial t} + \frac{\partial F_j(U)}{\partial x_j} = \frac{\partial F_{v,j}(U)}{\partial x_j} + S_T(U) + S_{\nabla\cdot\mathbf{B}}(U) + S_{\text{pellet}}(U), \tag{1}$$

where the solution vector $U \equiv U(x_1, x_2, x_3, t) \equiv U(R, z, R_0\phi, t)$ is $U = \{\rho, \rho u_i, B_i, e\}^{\mathrm{T}}$, and the flux vector $F_j(U)$ is given by

$$F_j(U) = \left\{ \begin{array}{c} \rho u_j \\ \rho u_i u_j + p_t \delta_{ij} - B_i B_j + B_T B_3 \delta_{ij} - B_i B_T \delta_{3j} - B_j B_T \delta_{i3} \\ u_j B_i - u_i B_j + B_T \delta_{i3} u_j - B_T \delta_{3j} u_i \\ (e + p + \frac{1}{2} B_k B_k) u_j - B_j (B_k u_k) + B_T B_3 u_j - (B_k u_k) B_T \delta_{3j} \end{array} \right\}. \tag{2}$$

In the above equations, R, z, ϕ, are the radial, axial and toroidal coordinates, R_0 is the major radius; ρ is the density, u_i is the velocity, B_i is the magnetic field, p and p_t are the pressure and total pressure, respectively, and e is the total energy per unit volume of the plasma. For numerical stability and robustness, we have subtracted out the equilibrium toroidal component of the initial equilibrium magnetic field, $B_T(x_i, 0) \equiv g_0/R$. These equations are closed by the perfect gas equation of state,

$$e = \frac{p}{\gamma - 1} + \frac{\rho}{2} u_k u_k + \frac{1}{2} B_k B_k, \tag{3}$$

which we note does not include the contribution $1/2B_T^2$. The flux vector $F_{v,j}(U)$ corresponds to the diffusive resistivity/viscosity terms and is omitted in the interest of brevity. The toroidal geometry terms are modeled in the

source terms as

$$S_T(U) = -\frac{1}{R}\begin{pmatrix} \rho u_R \\ \rho u_R^2 - \rho u_\phi^2 - B_R^2 + B_\phi^2 + 2B_\phi B_T \\ \rho u_R u_Z - B_R B_z \\ 2\rho u_R u_\phi - 2B_R B_\phi - 2B_R B_T \\ 0 \\ u_R B_z - B_R u_z \\ 0 \\ (e + p_t)u_R - (\mathbf{B}\cdot\mathbf{u})B_R + B_T B_\phi u_R \end{pmatrix} + \left(\frac{1}{R_0} - \frac{1}{R}\right)\frac{\partial F_\phi}{\partial \phi}. \tag{4}$$

For a large aspect ratio tokamak, $S_T(U)$ is small but it contains essential toroidal effects which cause the in–out asymmetry discussed in Section 4. The source terms $S_{\nabla\cdot\mathbf{B}}(U)$, written below,

$$S_{\nabla\cdot\mathbf{B}}(U) = -\nabla\cdot\mathbf{B}\left(\left\{0, B_R, B_z, B_\phi, u_R, u_z, u_\phi, u_z, (B\cdot u)\right\}^{\mathrm{T}}\right), \tag{5}$$

are included because we use the symmetrization procedure of Godunov [6] which leads to the 8-wave formulation. This formulation was also used by Powell et al. [7] in their AMR implementation of ideal MHD. Finally, the source terms $S_{\text{pellet}} = \{S_n/n_0, 0, 0, 0, 0, 0, 0, S_e/n_0\}^{\mathrm{T}}$, where n_0 is some reference number density, correspond to the mass source and energy source/sink terms, and are described next.

2.3. Pellet ablation model

In the present model, the pellet is described by a sphere of frozen molecular hydrogen of radius r_p. The trajectory $x_p(x_i, t)$ of the pellet is prescribed with a given initial location $x_{p0} \equiv x_p(x_i, 0)$ and constant velocity u_p. The density source term arises from the ablation of the pellet and is written in terms of number density (i.e. atoms per unit volume per unit time) as

$$S_n = \dot{N}\delta(x - x_p), \tag{6}$$

where the delta function is approximated as a Gaussian distribution centered over the pellet with a characteristic size equal to $10r_p$. The ablation rate of the pellet, originally derived by Parks and Turnbull [4] and modified for hydrogen pellets by Kuteev [8] is given below (in atoms/sec)

$$\dot{N} = -4\pi r_p^2 \frac{\mathrm{d}r_p}{\mathrm{d}t} 2n_m = 1.12\times 10^{16} n_e^{0.333} T_e^{1.64} r_p^{1.33} M_i^{-0.333}, \tag{7}$$

where n_e is the background plasma density in cm^{-3}, T_e is the background plasma electron temperature in eV, M_i is the atomic mass number in atomic units and $n_m = 2.63\times 10^{22}/\mathrm{cm}^3$ is the molecular density of frozen hydrogen. A useful approximation which eliminates the electron timescale from the problem is to consider the electron heat flux as being instantaneous compared to the other processes being computed. The time-asymptotic effect of the large electron heat flux is to make the temperature uniform along field lines, i.e. $T \equiv T(\psi)$. Thus, for single fluid equations, the temperature $T(\psi)$ in the volume V_ψ between flux surfaces ψ and $\psi + \mathrm{d}\psi$ will equilibrate as the density changes while still conserving energy in the volume V_ψ. This leads to the following energy source terms in the energy equation

$$S_e = 3\left(S_n T(\psi) + n\dot{T}(\psi)\right). \tag{8}$$

The first term in S_e corresponds to the localized increase in energy due to the heating of the ablated pellet mass, while the second term corresponds to a global adiabatic cooling of the entire flux surface. In practice, we compute the contribution due to the second term by separately solving a 1D model for the pellet injection assuming only classical processes are present. We then use table lookup and interpolation to compute the term $\dot{T}(\psi)$ in our 3D AMR simulation.

2.4. Initial and boundary conditions

The initial condition is a static equilibrium state. The initial magnetic field is written in terms of two function $\psi(R,z)$ and $g(R,z)$, i.e.

$$B = \frac{1}{R}(\hat{\phi} \times \nabla\psi + g\hat{\phi}). \tag{9}$$

These functions satisfy the Grad–Shafranov equation,

$$R\frac{\partial}{\partial R}\frac{1}{R}\frac{\partial\psi}{\partial R} + \frac{\partial^2\psi}{\partial z^2} + R^2\frac{\mathrm{d}p}{\mathrm{d}\psi} + g\frac{\mathrm{d}g}{\mathrm{d}\psi} = 0, \tag{10}$$

where $p \equiv p(\psi)$ and $g \equiv g(\psi)$. For a torus with rectangular cross-section of radial extent $2a$ and axial extent of $2b = 2\kappa a$ we may write $\psi(R,z) = f(R)\cos(\pi z/\kappa a)$. Further, with $g(R,z) = g_0 = \text{constant}$ we get

$$R\frac{\mathrm{d}}{\mathrm{d}R}\left(\frac{1}{R}\frac{\mathrm{d}f}{\mathrm{d}R}\right) + \left(\frac{R_0\pi}{a}\right)^2\left(\alpha R^2 - \frac{1}{4\kappa^2}\right)f = 0, \tag{11}$$

which permits a Frobenius-type series solution. The value of α is determined by imposing the boundary conditions $\psi = 0$. The pressure is written as $p = \bar{p} + p_0\psi^2$ where $\bar{p}$ is a small background pressure to avoid zero ion-acoustic speeds and $p_0 = \alpha\pi^2/(2a^2R_0^2)$. The toroidal field function $g_0 = R_0\alpha\pi^2|\psi|_{\max}q_0/(2ab)$, where q_0 (≈ 1) is the on-axis safety factor. Boundary conditions imposed are perfectly conducting walls in the radial/axial directions and periodic in the toroidal direction. In our simulations we use $\kappa = 1$, $a/R_0 = \pi/9$, for which $\alpha = 0.481509$.

3. Numerical method

In this section, we focus on the evaluation of the hyperbolic flux terms ($F_j(U)$) in Eq. (1). We use a finite volume technique wherein each variable is stored at the cell center. The numerical fluxes of conserved quantities are obtained at the cell faces using a combination of the 8-wave formulation [6] and unsplit upwinding [9,10]. We define a vector of "primitive" variables $W = \{\rho, u_i, B_i, p\}^{\mathrm{T}}$. Given the conserved quantities and all the source terms, i.e. $U_{\boldsymbol{i}}^n$, $S_{\boldsymbol{i}}^n$ (in this notation, $\boldsymbol{i}$ is a 3-tuple corresponding to the three dimensions), we want to compute a second-order accurate estimate of the fluxes: $F_{\boldsymbol{i}+\boldsymbol{e}^d/2}^{n+1/2}$ (d indicates the dth direction, $0 \leqslant d \leqslant 2$). The first step is to compute $W_{\boldsymbol{i}}^n$ in each cell, followed by fitting a linear profile in each cell subject to slope limiting. We then extrapolate the primitive and conserved variables at the cell faces using the normal derivative terms and the source terms at the cell centers, as follows.

$$W_{\boldsymbol{i},\pm,d} = W_{\boldsymbol{i}}^n + \frac{1}{2}\left(\pm I - A_{\boldsymbol{i}}^d\frac{\Delta t}{h}\right)P_{\pm}\Delta^d W_{\boldsymbol{i}}, \qquad U_{\boldsymbol{i},\pm,d} = U(W_{\boldsymbol{i},\pm,d}) + \frac{\Delta t}{2}S_{\boldsymbol{i}}^n, \tag{12}$$

where $A_{\boldsymbol{i}}^d = (\nabla_W U\nabla_W F^d)(W_{\boldsymbol{i}})$ and $P_{\pm}(W) = \sum_{\pm\lambda_k>0}(l_k \cdot W)r_k$, and $\Delta^d W_{\boldsymbol{i}}$ is the undivided but limited slope. The eigenvalues, and left and right eigenvectors of $A_{\boldsymbol{i}}^d$ are λ_k, l_k, and r_k, respectively with $k = 1\ldots8$ in the eight-wave formulation (see Powell et al. [7] for the left and right eigenvectors). We compute corrections to $U_{\boldsymbol{i},\pm,d}$ corresponding to one set of transverse derivatives appropriate to obtain $(1,1,1)$ diagonal coupling:

$$U_{\boldsymbol{i},\pm,d_1,d_2} = U_{\boldsymbol{i},\pm,d_1} - \frac{\Delta t}{3h}\left(F_{\boldsymbol{i}+\boldsymbol{e}^{d_2}/2}^{1\mathbf{D}} - F_{\boldsymbol{i}-\boldsymbol{e}^{d_2}/2}^{1\mathbf{D}}\right), \quad d_1 \neq d_2,\ 0 \leqslant d_1, d_2 < 3, \tag{13}$$

where $F_{\boldsymbol{i}\pm\boldsymbol{e}^d/2}^{1\mathbf{D}} = \mathrm{RP}(U_{\boldsymbol{i},+,d}, U_{\boldsymbol{i}+\boldsymbol{e}^d,-,d})$. The notation $F = \mathrm{RP}(U_L, U_R)$ implies that the flux F is evaluated by solving a linearized Riemann problem using U_L and U_R as left and right states, respectively. We next compute

final corrections to $U_{\boldsymbol{i},\pm,d}$ due to transverse derivatives:

$$U^{n+1/2}_{\boldsymbol{i},\pm,d} = U_{\boldsymbol{i},\pm,d} - \frac{\Delta t}{2h}\left(F_{\boldsymbol{i}+\boldsymbol{e}^{d_1}/2,d_2} - F_{\boldsymbol{i}-\boldsymbol{e}^{d_1}/2,d_2}\right), \tag{14}$$

where $F_{\boldsymbol{i}+\boldsymbol{e}^{d_1}/2,d_2} = \mathrm{RP}(U_{\boldsymbol{i},+,d_1,d_2}, U_{\boldsymbol{i}+\boldsymbol{e}^{d_1},+,d_1,d_2})$, and $0 \leqslant d < 3$; $d_1 \neq d_2 \neq d$. At this stage, we solve another Riemann problem at the cell faces using $U^{n+1/2}_{\boldsymbol{i},+,d}$ and $U^{n+1/2}_{\boldsymbol{i}+\boldsymbol{e}^d,-,d}$ as the left and right states, respectively. The magnetic field obtained from the solution to the Riemann problem at $n+1/2$ at the cell faces is not guaranteed to be divergence free. We enforce the solenoidal property of the magnetic field by a MAC projection, using **B** at the cell faces to obtain a cell-centered monopole charge density. A Poisson solver is used to find a scalar field satisfying $\nabla^2\chi = \nabla\cdot\mathbf{B}$ with Neumann boundary conditions in the radial/axial directions and periodic in the toroidal direction. The magnetic field at the cell faces is then corrected according to $B^{n+1/2}_{\boldsymbol{i}+\boldsymbol{e}^d/2} = B^{n+1/2}_{\boldsymbol{i}+\boldsymbol{e}^d/2} - \nabla\chi$. Finally the fluxes at cell faces are obtained as $F^{n+1/2}_{\boldsymbol{i}+\boldsymbol{e}^d/2} = F(U^{n+1/2}_{\boldsymbol{i}+\boldsymbol{e}^d/2})$ and the conserved quantity at the cell centers are updated using these fluxes. The Poisson equation in the projection step above is cast in a residual-correction form and solved using a multi-grid technique on each level in the AMR hierarchy. The residual smoothing is a Gauss–Seidel relaxation procedure with red-black ordering. When meshes cannot be coarsened any further, the Poisson solve is taken to convergence using a bottom-smoother which is a biconjugate gradient solver. We implemented the above method into the *Chombo* framework and have developed a second-order adaptive parallel MHD code. Chombo is a collection of C++ libraries for implementing block-structured AMR finite difference calculations [11]. Particular care is taken in implementing coarse-fine interface interpolations of appropriate order to ensure second-order accuracy. Furthermore, conservation at coarse-fine interfaces is maintained by flux-refluxing. This leads to a non-zero cell-centered $\nabla\cdot\mathbf{B}$ in coarse cells which are adjacent to coarse-fine boundaries, which being a set of codimension one does not significantly affect the accuracy of the solution.

4. Simulation results

In this section, we present preliminary results from early to intermediate stages of pellet injection. The results discussed here correspond to a midpoint toroidal field of $0.23T$, $\beta \approx 0.1$, and a pellet of 1 mm radius moving radially with a velocity of 3200 m/s in a tokamak with minor radius of $a = 0.26$ m. Two cases are discussed: one in which the pellet is initialized on the high field side (HFS or the so-called inside launch case) and the other in which the pellet is injected from the low field side (LFS or the "outside" launch case). Because the temperature of the plasma is low near the edges of the tokamak, we initialize the pellet at some radial distance inside the tokamak. This is merely to save computational effort and have interesting dynamics take place relatively quickly. In both the LFS and the HFS case, the initial location of the pellet is on the same flux surface so that the pellet encounters the same initial temperature in both the LFS and HFS cases. Based on preliminary tests which suggested that the energy sink term provides only a small contribution, but is nonetheless computationally expensive to evaluate and occasionally leads to noisy solutions, we omitted the sink term in the results presented here.

Fig. 1 shows a density isosurface, viewed radially inwards, at times $t = 2, 20, 60$ (time is normalized by the Alfvén time) for the HFS case. The outlines of the various meshes in the calculation are also shown in Fig. 1. At $t = 2$ the pellet ablated mass is roughly in the shape of an ellipsoid with its major axis aligned along the magnetic field lines. The pellet cloud is a localized region of high β with the dominant mass motion being along the magnetic field lines. As time progresses, the ablated mass moves parallel to the magnetic field at speeds of about one-third of the local acoustic speed. (See scatter plots of β vs. density in Fig. 2 and local Mach number vs. density in Fig. 3.) In addition to the "classical" parallel transport there is clear evidence of "anomalous" transport perpendicular to the flux surfaces.

We now examine this phenomenon in more detail and compare and contrast between HFS and LFS pellet launches. Fig. 4 shows poloidal slices at the mean toroidal pellet location for the HFS and LFS cases. At time

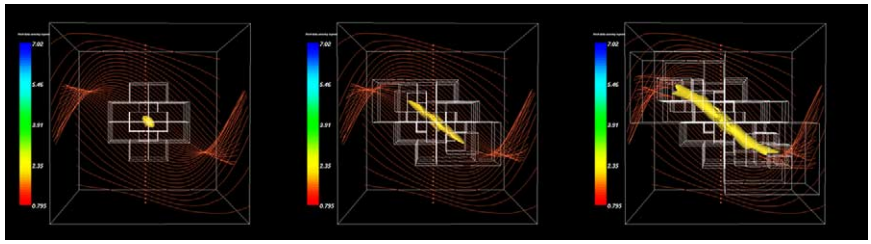

Fig. 1. Density isosurface ($\rho = 2$) for a HFS pellet launch. (a) $t = 2$, (b) $t = 20$, (c) $t = 60$ viewed radially inwards. The magnetic field lines are shown in red. The box outlines depict the meshes. Time is normalized by the Alfvèn wave transit time. (Note that although the domain is a torus the visualizations are presented in a cube.)

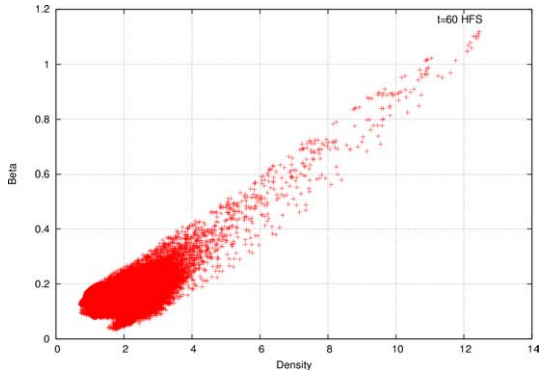

Fig. 2. Scatter plot of β vs. ρ at $t = 60$ for the HFS launch. High β is strongly correlated with high density.

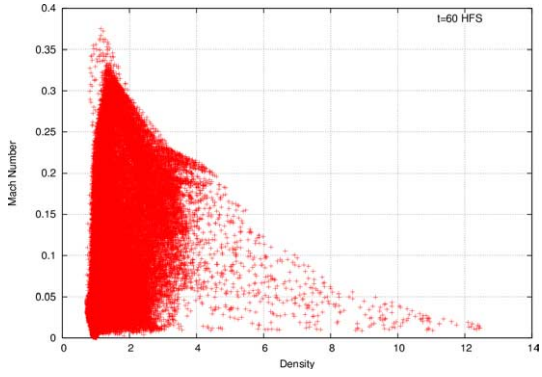

Fig. 3. Scatter plot of local Mach number vs. ρ at $t = 60$ for the HFS launch.

$t = 2$ we observe the ablated mass in a cloud around the mean pellet position. At later times ($t = 20, 60$), the pellet ablated mass has a significant outward radial displacement compared to the mean pellet location.

The LFS case shows a dramatic turning around of the mass due to the zero mass flux boundary conditions (Fig. 4(b3)) It is conjectured that an outflow boundary condition would lead to a substantial loss of the ablated mass and thus poor fueling efficiency in the LFS case. The observed outward displacement implies that HFS launches are more favorable for refueling tokamaks as opposed to the LFS launches, consistent with observed behavior in experiments [1,12]. We may reconcile this seemingly "anomalous" transport by appealing to the model by Parks [13] which notes that magnetic curvature and ∇B-induced charged particle drifts cause a local separation

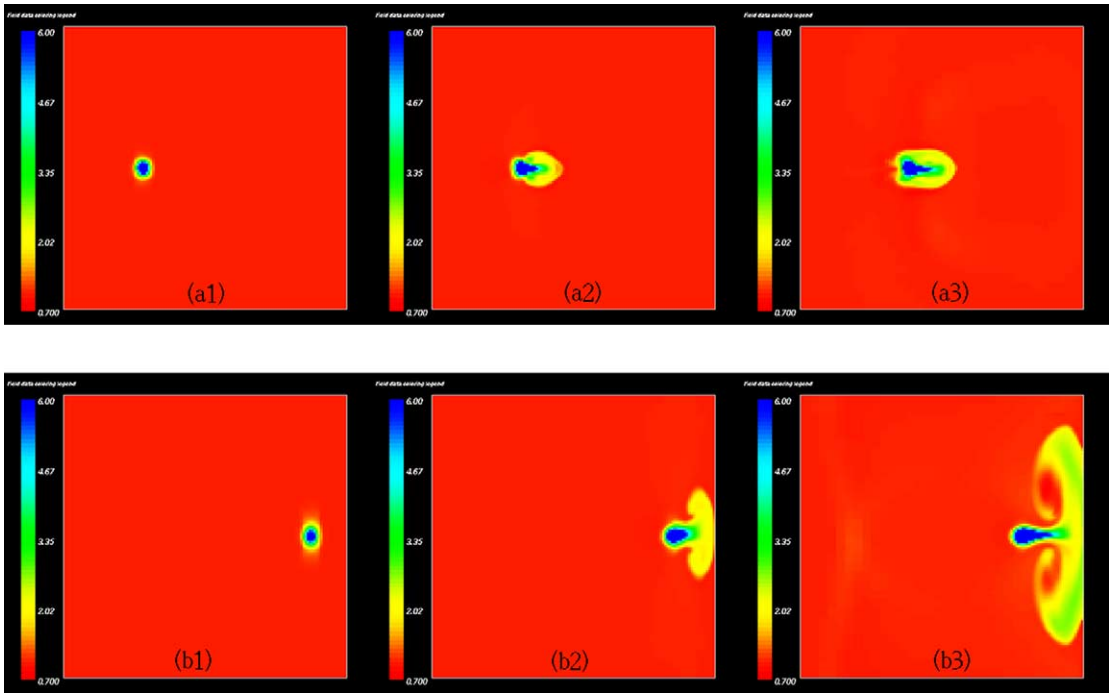

Fig. 4. Density field in a poloidal cross-section. (a1) HFS $t = 2$, (a2) HFS $t = 20$, (a3) HFS $t = 60$, (b1) LFS $t = 2$, and (b2) LFS $t = 20$, and (b3) LFS $t = 60$.

of charges in the pellet cloud. This leads to an axially-oriented electric field, and so the $E \times B$ drift is radially outward in both the LFS and the HFS case.

It is instructive to examine the flow pattern of the perpendicular drift velocity $v_\perp = E \times B/|B|^2$. The radial component of $v_\perp$ is the dominant one and is shown in Fig. 5 in a poloidal slice. For the HFS case, in Fig. 5(a), there is a dominant outward radial $v_\perp$ carrying the bulk of the pellet mass outward. This is flanked on either side in the axial direction by inward radial motion resulting in a nearly incompressible flow pattern. So the simple picture of only outward radial $v_\perp$ drift is augmented by this somewhat smaller turning around of the mass which leads to the mushroom-shaped structure in the poloidal plane.

For the LFS case too, the outward radial $E \times B$ drift grows with time and is clearly seen in Fig. 5(b). The perpendicular transport of the ablated mass brings into question some of the assumptions made in the earlier section. In calculation of the ablation rate, we assumed that the ablated mass is heated instantaneously to the flux surface temperature. However, the motion of the ablated mass radially outwards in the HFS case means that the temperature the pellet encounters will actually be smaller than that assumed. Furthermore, the energy sink term in the equations, which are based on a one-dimensional parallel transport model will need to be modified.

5. Conclusion and future work

In this paper, we presented a numerical method which is based on an unsplit upwinding method coupled with the eight-wave formulation. A MAC-projection scheme is implemented to enforce the solenoidal property of the magnetic field. This projection requires the solution of a Poisson equation which is solved using a multi-grid technique. It was observed that the convergence of the Poisson solver was sensitive to the block-size in the AMR mesh-hierarchy. A pellet injection model was implemented as a source term in the density equations and

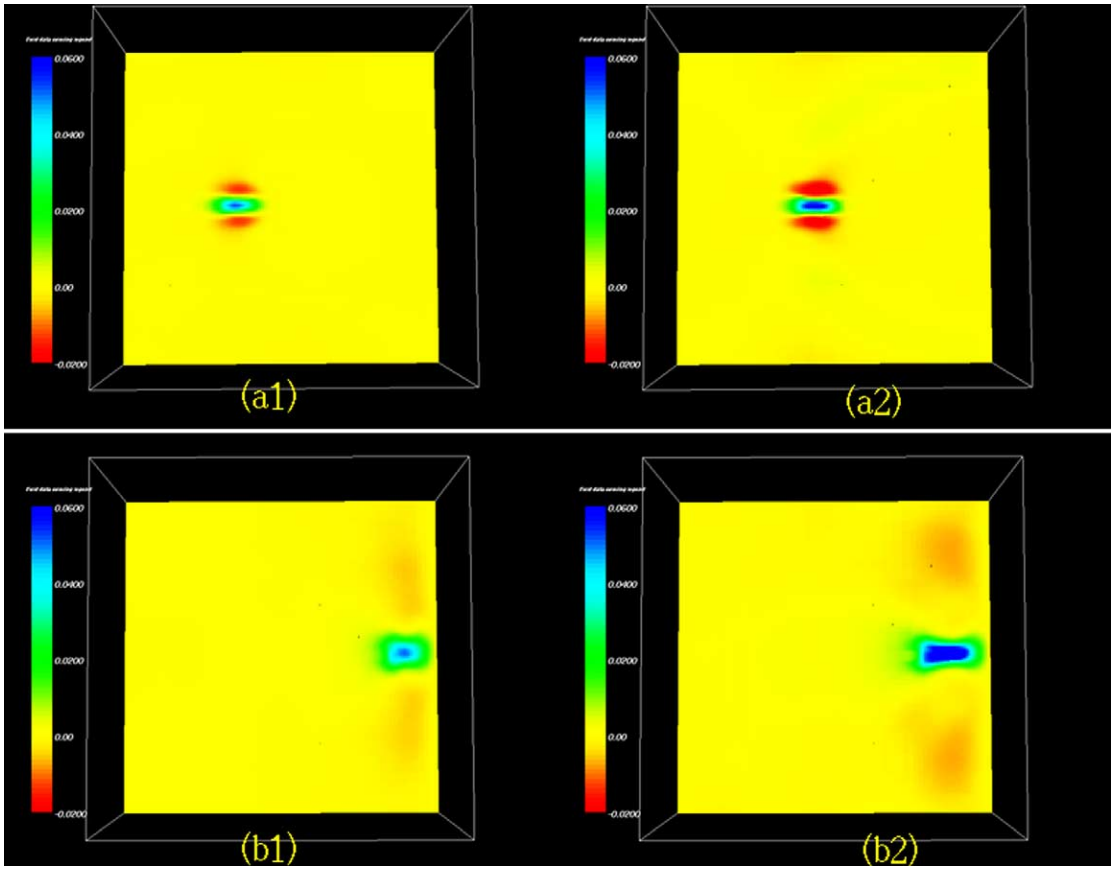

Fig. 5. Perpendicular drift velocity $v_\perp$ in a Poloidal cross-section. (a1) HFS $t = 20$, (a2) HFS $t = 60$, (b1) LFS $t = 20$, and (b2) LFS $t = 60$.

corresponding energy sources and sinks in the energy equation. AMR simulations of the pellet injection process were carried out for the inside and outside launch cases. Preliminary studies indicate that AMR provides a speed-up exceeding two orders of magnitude over corresponding uniform mesh simulations essential to accurately resolve the physical processes involved in pellet injection. AMR is an effective way of achieving computational efficiency in detailed and resolved simulations of the pellet injection process. It was observed that the pellet ablated mass is dominantly transported along magnetic field lines but that a $E \times B$ drift causes a significant outward radial motion of the pellet cloud in both the LFS and HFS cases. A high resolution numerical simulation is a viable method of computing the relative importance of these two competing phenomena for redistributing the pellet mass.

The results presented in this paper did not include resistive terms which will be included in future work. We also plan to develop models which better account for the rapid electron heating and corresponding cooling terms in the energy equation, taking into account the perpendicular transport of the ablated mass. Finally, we plan to undertake resolved simulations of pellet injection with more realistic physical parameters, and to investigate other launch locations in addition to the HFS and LFS pellet injections.

Acknowledgements

The authors benefited from useful discussions with Drs. W. Park, P. Parks, H. Strauss, and G. Schmidt. This work was supported by USDOE Contract no. DE-AC020-76-CH03073. This research used resources of the National

Energy Research Scientific Computing Center, which is supported by the Office of Science of the U.S. Department of Energy under Contract No. DE-AC03-76SF00098.

References

[1] L. Baylor, et al., Phys. Plasmas 32 (2000) 1878.
[2] L. Baylor, et al., J. Nucl. Matter 313 (2003) 530.
[3] H.R. Strauss, W. Park, Phys. Plasmas 5 (1998) 2676.
[4] P.B. Parks, R.J. Turnbull, Phys. Fluids 21 (1978) 1735.
[5] A.K. Macaulay, Nuclear Fusion 34 (1994) 43.
[6] S.K. Godunov, Numer. Methods Mech. Contin. Media 1 (1972) 26.
[7] K.G. Powell, et al., J. Comput. Phys. 154 (1999) 284–309.
[8] B.V. Kuteev, Nuclear Fusion 35 (1995) 431.
[9] P. Colella, J. Comput. Phys. 87 (1990) 171–200.
[10] R. Crockett, et al., J. Comput. Phys. (2003) submitted for publication.
[11] http://seesar.lbl.gov/ANAG/chombo.
[12] P.T. Lang, et al., Phys. Rev. Lett. 79 (1997) 1487.
[13] P.B. Parks, W.D. Sessions, L.R. Baylor, Phys. Plasmas 7 (2000) 1968.